Distinct gene clusters drive formation of ferrosome organelles in bacteria

Carly Grant, Matthieu Amor, Hector Trujillo, Sunaya Krishnapura, Anthony Iavarone, Arash Komeili

Ferrosomes are iron storage organelles formed by distinct gene clusters

Carly R. Grant[1], Matthieu Amor[2], Hector A. Trujillo[1], Sunaya Krishnapura[1], Anthony T. Iavarone[3], and Arash Komeili[1]

[1]Department of Plant and Microbial Biology, University of California, Berkeley, USA
[2]Aix-Marseille Université, CEA, CNRS, BIAM, 13108 Saint-Paul-lez-Durance, France
[3]QB3/Chemistry Mass Spectrometry Facility, University of California, Berkeley, USA

Cellular iron homeostasis is vital and maintained through tight regulation of iron import, efflux, storage, and detoxification[1–3]. The most common modes of iron storage employ proteinaceous compartments, such as ferritins and related proteins[4,5]. While lipid-bounded iron compartments have also been described, the basis for their formation and function remains unknown[6,7]. Here, we focus on one such compartment, which we have named the 'ferrosome', that was previously observed in the anaerobic bacterium *Desulfovibrio magneticus*[6]. Using a proteomic approach, we identify three ferrosome-associated (Fez) proteins that are responsible for forming ferrosomes in *D. magneticus*. The Fez proteins are encoded in a putative operon and include FezB, a P_{1B-6}-ATPase found in phylogenetically and metabolically diverse species of bacteria and archaea. We show that two other species, *Rhodopseudomonas palustris* and *Shewanella putrefaciens*, make ferrosomes through the action of their six-gene *fez* operon. Additionally, we find that *fez* operons are sufficient for ferrosome formation in foreign hosts. Using *S. putrefaciens* as a model, we show that ferrosomes likely play a role in the anaerobic adaptation to iron starvation. Overall, this work establishes ferrosomes as a new class of iron storage organelles and sets the stage for studying ferrosome formation and structure in diverse microorganisms.

D. magneticus strain RS-1 is an anaerobic sulfate-reducing bacterium and an emerging model organism for studying the natural diversity of magnetite (Fe_3O_4) biomineralization within an organelle termed the magnetosome[8,9]. Independent of magnetosomes, *D. magneticus* makes subcellular electron-dense granules rich in iron, phosphorus, and oxygen that are enclosed by a lipid-like membrane[6]. These granules, which we propose to name 'ferrosomes' for 'iron bodies', are visible by transmission electron microscopy (TEM) after *D. magneticus* transitions out of iron starvation with the supplementation of iron[6]. Depending on the concentration of iron

supplemented, ferrosomes range in size from about 12 to 65 nm and increase in size over time (Extended Data Fig. 1). We had previously found that the iron accumulated in ferrosomes is not sufficient for magnetosome formation and that magnetosome genes are not required for ferrosome formation[6,10]. While these studies support the hypothesis that the ferrosome is a distinct organelle, the molecular basis for ferrosome formation and function has remained a mystery.

To understand the mechanistic basis of ferrosome formation, we isolated ferrosomes from cell lysates through a sucrose cushion and used mass spectrometry to identify their associated proteins (Extended Data Fig. 2a-c). Mass spectrometry analysis revealed three proteins highly enriched in the ferrosome fraction, DMR_28330 (FezB), DMR_28340 (FezC), and DMR_28320 (FezA), that are encoded by genes arranged in a putative operon, *fezABC* (Fig. 1a, b) (gene prefix given for the phonetic pronunciation 'ferrozome'). Of these three proteins, only FezB has a functional annotation: a heavy metal-transporting P_{1B}-ATPase. P_{1B}-ATPases are a large family of integral membrane proteins that transport metals across membranes using the energy of ATP hydrolysis[11]. FezB falls within the P_{1B-6}-ATPase group, an uncharacterized subfamily with unique transmembrane topology and a possible role in iron transport based on genomic context in several species[12]. FezB has the cytoplasmic domains characteristic of all P_{1B}-ATPases and unique motifs in the transmembrane domains responsible for metal specificity[11–13] (Fig. 1b, Extended Data Fig. 3). FezC has an N-terminal heavy-metal associated (HMA) domain annotation and two predicted transmembrane domains while FezA has a hydrophobic N-terminal region (Extended Data Fig. 2d-f). The putative transmembrane domains of FezA, FezB, and FezC are consistent with our earlier observations that ferrosomes are surrounded by a lipid-like

membrane[6]. Additionally, the characteristics of metal binding and transport domains suggest that the *fez* genes are the blueprint for ferrosome formation and function.

To test this hypothesis, we deleted the *D. magneticus fezB* and *fezC* genes through allelic replacement with a streptomycin-resistance cassette. The resulting mutant, Δ*fezBC*$_{Dm}$, could still form magnetosomes but was unable to form ferrosomes (Fig. 1d). Complementation of Δ*fezBC*$_{Dm}$ with *fezABC*$_{Dm}$ (Δ*fezBC::fezABC*) rescued the formation of ferrosomes, which were on average smaller than those in wild-type (WT) *D. magneticus* (Fig. 1c-f). The smaller ferrosome size, which is also observed in WT *D. magneticus* when induced to form ferrosomes with a lower concentration of iron (Extended Data Fig. 1f, j), could be due to less iron being stored in individual ferrosomes. In addition, expression of *fezABC*$_{Dm}$ *in trans* in either the WT or the Δ*fezBC*$_{Dm}$ mutant led to constitutive ferrosome production in iron replete growth medium with no effect on magnetosome formation (Extended Data Fig. 4). Thus, ferrosomes are a structurally and genetically distinct organelle in *D. magneticus*.

We next asked if other organisms were also capable of forming ferrosomes. Phylogenetic analysis of FezB revealed a clear group of its homologs that share signature motifs in the putative metal binding transmembrane domains (D[Y/F]SCA and HNxxT, respectively) which define the P_{1B-6}-ATPase subgroup[12] (Fig. 1g, Supplementary Table 1). While FezB homologs lack a known cytoplasmic N-terminal metal binding domain, we found a notable ‘R-rich’ motif containing two or more arginine residues spaced by a variable residue (e.g. RxR or RxRxR) in the N-terminus of the majority of FezB homologs (Fig. 1g, Supplementary Table 1). We also identified this R-rich motif in related P_{1B}-ATPases, including CtpC, a metal transporter that contributes to *M. tuberculosis* virulence[14,15]. Proteins identified in this study as FezB homologs, as well as related P_{1B}-ATPases with an R-rich motif, were previously assigned to a family of

functionally uncharacterized P-type ATPases named FUPA32[13]. FezB homologs are found in diverse species of bacteria and archaea that inhabit a range of environmental and host-associated habitats. While metabolically diverse, the majority of these species are strict or facultative anaerobes (Supplementary Table 2). Despite the wide distribution of FezB homologs in bacteria, only two other magnetosome-forming bacteria, including *Magnetospirillum gryphiswaldense* strain MSR-1 and *Magnetospirillum sp.* SO-1, have an apparent FezB homolog.

In most species *fezB* lies in a conserved gene cluster (Extended Data Fig. 5a). Upon closer inspection we found that nearly all *fez* gene clusters have one or more proteins that have a hydrophobic region with a conserved GxxxG motif (Fig. 1h, Extended Data Fig. 5b, 6b, Supplementary Table 4). GxxxG motifs are common in transmembrane domains where they may facilitate protein-protein interactions and have even been shown to induce local curvature and tubulation of membranes[16–18]. Many *fez* gene clusters also encode one or more proteins with an N-terminal R-rich motif similar to that found in FezB (Extended Data Fig. 5b, 6a, Supplementary Table 5). These proteins include both soluble and membrane proteins, including FezC (Extended Data Fig. 6a). In some of the larger *fez* gene clusters, we discovered a second uncharacterized P_{1B}-ATPase (FezH) with an R-rich motif and distinct transmembrane metal binding sites (Fig. 1g, h, Extended Data Fig. 6a, Supplementary Table 3). Conserved proteins also include a DUF4405 protein with homology to the membrane domains of FezC, a FeoA-domain containing protein, and a DUF2202 ferritin-like protein with a C-terminal GxxxG motif (Fig. 1h, Extended Data Fig. 5b, 6, Supplementary Table 6). These predicted motifs, as well as the genomic association of *fez* gene clusters with iron homeostasis genes[12] (Extended Data Fig. 5c, Supplementary Table 7), supports a model in which a complex of Fez proteins transport iron into ferrosomes for storage.

The broad phylogenetic distribution of *fez* gene clusters suggests that diverse species of bacteria and archaea might be capable of forming ferrosomes. Since most of these organisms are uncultured or difficult to manipulate in the lab, we searched for culturable bacteria with established tools for genetic manipulation to serve as models for ferrosome formation. In addition to being genetically tractable, the Gammaproteobacterium *S. putrefaciens* strain CN-32 has been reported to form membrane-enclosed electron-dense granules consisting of mixed-valence iron, phosphorus, and oxygen[7,19]. These granules could not be found in several other *Shewanella* species[19]. Amongst the *Shewanella* species tested in these studies, *S. putrefaciens* is the only one with a putative *fez* operon (Fig. 1h, Fig. 2a). Thus, we hypothesized that the iron-containing granules observed in previous studies are analogous to ferrosomes made by *D. magneticus*.

As described in previous work, we found that *S. putrefaciens* forms electron-dense granules when respiring hydrous ferric oxide (HFO) and/or fumarate in growth medium supplemented with iron (Fig. 2b, Extended Data Fig. 7a, b)[7,19]. Unlike the previous studies, we used a rich broth rather than a defined growth medium for all growth conditions. Likewise, the Alphaproteobacterium *R. palustris* strain CGA009, which has a similar *fez* operon to *S. putrefaciens* (Fig. 1h), forms electron-dense granules resembling ferrosomes when grown photoheterotrophically in anaerobic medium supplemented with iron (Extended Data Fig. 7c, d). This is in accordance with previous proteomic and transcriptomic studies that show *fez* genes are expressed during anaerobic conditions in *R. palustris* strains CGA009 and TIE-1[20–22]. To confirm that the granules in *S. putrefaciens* and *R. palustris* are ferrosomes, we made markerless deletions of their *fez* gene clusters (Δfez_{Sp} and Δfez_{Rp}, respectively). Both the Δfez_{Sp} and Δfez_{Rp} mutants no longer made granules and complementation by expressing their respective *fez* gene

cluster *in trans* rescued the phenotype (Fig. 2b-d, Extended Data Fig. 7e-j). Similar to *D. magneticus*, the ferrosomes observed after complementation were smaller than those in the WT cells (Fig. 3l).

We next asked whether or not *fez* genes can lead to ferrosome formation in a naïve host. To answer this question, we heterologously expressed *fez* gene clusters in *E. coli*. When grown anaerobically in medium supplemented with iron, *E. coli* expressing fez_{Sp} (*E. coli* fez_{Sp}^{+}) had a visibly dark pellet whereas the control cultures and cultures grown without iron had a white pellet (Fig. 3a-d). While no obvious growth phenotype was observed in *E. coli* fez_{Sp}^{+} cells, TEM revealed electron-dense granules in *E. coli* fez_{Sp}^{+} cells grown with iron that were not found in *E. coli* cells carrying a control plasmid (Fig. 3e-g). The granules have an average diameter of around 20 nm (Fig. 3l), which is nearly double that of the proteinaceous iron storage compartments found naturally in *E. coli*[1]. To ensure that the granules observed in *E. coli* contained iron, we analyzed their elemental composition using Energy Dispersive X-ray Spectroscopy (EDS) coupled to TEM and compared the spectra to ferrosomes in WT *S. putrefaciens*. While spectra obtained for *E. coli* fez_{Sp}^{+} and *S. putrefaciens* showed similar chemical patterns, iron could only be detected when EDS analyses were focused on ferrosomes in both strains (Fig. 3h, i, Extended Data Fig. 8), demonstrating that iron was specifically accumulated in these structures. Attempts to produce ferrosomes in *E. coli* through expression of the *R. palustris* and *D. magneticus fez* genes were unsuccessful, perhaps due to their more distant evolutionary relationship.

Using another naïve host, we found that the magnetosome-forming Alphaproteobacterium *M. magneticum* strain AMB-1 also formed granules resembling ferrosomes when expressing the *R. palustris fez* operon (*M. magneticum* fez_{Rp}^{+}) (Fig. 3j, k). These ferrosome-like granules in *M.*

magneticum fez_{Rp}^{+} could be distinguished from magnetosomes because they were not aligned with magnetosomes and they appeared less dense (Fig. 3k). Magnetite crystals in *M. magneticum* magnetosomes also showed sharp edges clearly distinct from the amorphous ferrosomes[6]. The ferrosome-like particles observed in *M. magneticum* fez_{Rp}^{+} were, on average, larger than those in *E. coli* fez_{Sp}^{+} (Fig. 3l). This could in part be due to the large pool of intracellular dissolved iron in *M. magneticum*, which is 10-100-fold higher than that in *E. coli*[23]. In summary, these results show that *fez* genes are necessary and sufficient for ferrosome formation in diverse bacteria.

The genetic components of *fez* gene clusters, patterns of ferrosome formation, and iron accumulation in ferrosomes point to a role for this organelle in iron homeostasis. In other systems, iron storage compartments are important for surviving iron starvation. Using *S. putrefaciens* as a model, we found that addition of the iron chelator EDTA impaired aerobic and anaerobic growth for both the WT and the Δfez_{Sp} strains (Extended Data Fig. 9a). When grown aerobically, where no ferrosomes are formed[7], the WT and Δfez_{Sp} strains showed no difference in growth (Extended Data Fig. 9a). However, when grown anaerobically with EDTA the Δfez_{Sp} mutant had a longer lag phase compared to WT (Fig. 2e, Extended Data Fig. 9b)—a phenotype that is complemented in the Δfez_{Sp}::fez_{Sp} strain (Fig. 2f). The growth defects observed from the addition of EDTA were rescued by adding equimolar concentrations of iron (Fig. 2g), suggesting that this phenotype is specifically due to iron limitation induced with EDTA. Overall, these results mirror the iron storage defect reported in the *E. coli* ferritin mutant during aerobic growth[24]. They are also consistent with recent findings that lag phase is a growth period dominated by accumulation of metals, such as iron, needed for the heavy enzymatic burden of exponential phase[25]. Therefore, we propose that ferrosomes in *S. putrefaciens* likely function to store iron during anaerobic metabolism which can be accessed under severe iron starvation

conditions. Further work is needed to show if this function is universal in all ferrosome-forming bacteria.

In summary, our study reveals the genetic requirement for ferrosome formation and provides evidence that it functions as an iron storage organelle during anaerobic metabolism. Our findings that Fez proteins, which have putative membrane domains, are associated with isolated ferrosomes and are required for ferrosome function support two independent studies that found lipid-like membranes surrounding ferrosomes[6,7]. This is in stark contrast to all other previously described bacterial and archaeal systems that depend on proteinaceous compartments for iron storage[4,5]. While this study focused on environmental bacteria, iron storage may be a universal function of ferrosomes, including in host-associated bacteria. This hypothesis is supported by several unrelated studies in multiple bacteria that show *fez* gene expression is upregulated in low iron environments[26–31], including during infection by *Clostridium difficile*[32]. In the future, ferrosomes may prove to be a novel drug target for combating pathogenic bacteria. They may also be platforms for synthetic biomining and bioremediation applications that leverage their metal-accumulating capabilities.

References

1. Andrews, S. C. Iron Storage in Bacteria. In *Advances in Microbial Physiology* (ed. Poole, R. K.) vol. 40 281–351 (Academic Press, 1998).
2. Touati, D. Iron and Oxidative Stress in Bacteria. *Arch. Biochem. Biophys.* **373**, 1–6 (2000).
3. Andrews, S. C., Robinson, A. K. & Rodríguez-Quiñones, F. Bacterial iron homeostasis. *FEMS Microbiol. Rev.* **27**, 215–237 (2003).

4. Andrews, S. C. The Ferritin-like superfamily: Evolution of the biological iron storeman from a rubrerythrin-like ancestor. *Biochim. Biophys. Acta BBA – Gen. Subj.* **1800**, 691–705 (2010).
5. Nichols, R. J., Cassidy-Amstutz, C., Chaijarasphong, T. & Savage, D. F. Encapsulins: molecular biology of the shell. *Crit. Rev. Biochem. Mol. Biol.* **52**, 583–594 (2017).
6. Byrne, M. E. *et al. Desulfovibrio magneticus* RS-1 contains an iron- and phosphorus-rich organelle distinct from its bullet-shaped magnetosomes. *Proc. Natl. Acad. Sci. U. S. A.* **107**, 12263–12268 (2010).
7. Glasauer, S., Langley, S. & Beveridge, T. J. Intracellular Iron Minerals in a Dissimilatory Iron-Reducing Bacterium. *Science* **295**, 117–119 (2002).
8. Sakaguchi, T., Arakaki, A. & Matsunaga, T. *Desulfovibrio magneticus* sp. nov., a novel sulfate-reducing bacterium that produces intracellular single-domain-sized magnetite particles. *Int. J. Syst. Evol. Microbiol.* **52**, 215–221 (2002).
9. Grant, C. R., Rahn-Lee, L., LeGault, K. N. & Komeili, A. Genome Editing Method for the Anaerobic Magnetotactic Bacterium *Desulfovibrio magneticus* RS-1. *Appl Env. Microbiol* **84**, e01724-18 (2018).
10. Rahn-Lee, L. *et al.* A Genetic Strategy for Probing the Functional Diversity of Magnetosome Formation. *PLOS Genet.* **11**, e1004811 (2015).
11. Argüello, J. M., Eren, E. & González-Guerrero, M. The structure and function of heavy metal transport P1B-ATPases. *BioMetals* **20**, 233 (2007).
12. Smith, A. T., Smith, K. P. & Rosenzweig, A. C. Diversity of the metal-transporting P_{1B}-type ATPases. *J. Biol. Inorg. Chem. JBIC Publ. Soc. Biol. Inorg. Chem.* **19**, 947–960 (2014).

13. Chan, H. *et al.* The P-Type ATPase Superfamily. *J. Mol. Microbiol. Biotechnol.* **19**, 5–104 (2010).
14. Padilla-Benavides, T., Long, J. E., Raimunda, D., Sassetti, C. M. & Argüello, J. M. A Novel P_{1B}-type Mn^{2+}-transporting ATPase Is Required for Secreted Protein Metallation in Mycobacteria. *J. Biol. Chem.* **288**, 11334–11347 (2013).
15. Botella, H. *et al.* Mycobacterial P_1-Type ATPases Mediate Resistance to Zinc Poisoning in Human Macrophages. *Cell Host Microbe* **10**, 248–259 (2011).
16. Russ, W. P. & Engelman, D. M. The GxxxG motif: a framework for transmembrane helix-helix association. *J. Mol. Biol.* **296**, 911–919 (2000).
17. Unterreitmeier, S. *et al.* Phenylalanine promotes interaction of transmembrane domains via GxxxG motifs. *J. Mol. Biol.* **374**, 705–718 (2007).
18. Jarsch, I. K., Daste, F. & Gallop, J. L. Membrane curvature in cell biology: An integration of molecular mechanisms. *J Cell Biol* **214**, 375–387 (2016).
19. Glasauer, S. *et al.* Mixed-Valence Cytoplasmic Iron Granules Are Linked to Anaerobic Respiration. *Appl. Environ. Microbiol.* **73**, 993–996 (2007).
20. VerBerkmoes, N. C. *et al.* Determination and Comparison of the Baseline Proteomes of the Versatile Microbe *Rhodopseudomonas palustris* under Its Major Metabolic States. *J. Proteome Res.* **5**, 287–298 (2006).
21. Rey, F. E. & Harwood, C. S. FixK, a global regulator of microaerobic growth, controls photosynthesis in *Rhodopseudomonas palustris*. *Mol. Microbiol.* **75**, 1007–1020 (2010).
22. Bose, A. & Newman, D. K. Regulation of the phototrophic iron oxidation (*pio*) genes in *Rhodopseudomonas palustris* TIE-1 is mediated by the global regulator, FixK. *Mol. Microbiol.* **79**, 63–75 (2011).

23. Amor, M. *et al.* Magnetotactic Bacteria Accumulate a Large Pool of Iron Distinct from Their Magnetite Crystals. *Appl. Environ. Microbiol.* **86**, (2020).
24. Abdul-Tehrani, H. *et al.* Ferritin Mutants of *Escherichia coli* Are Iron Deficient and Growth Impaired, and fur Mutants are Iron Deficient. *J. Bacteriol.* **181**, 1415–1428 (1999).
25. Rolfe, M. D. *et al.* Lag Phase Is a Distinct Growth Phase That Prepares Bacteria for Exponential Growth and Involves Transient Metal Accumulation. *J. Bacteriol.* **194**, 686–701 (2012).
26. Bender, K. S. *et al.* Analysis of a Ferric Uptake Regulator (Fur) Mutant of *Desulfovibrio vulgaris* Hildenborough. *Appl. Environ. Microbiol.* **73**, 5389–5400 (2007).
27. Uebe, R. *et al.* Deletion of a *fur*-Like Gene Affects Iron Homeostasis and Magnetosome Formation in *Magnetospirillum gryphiswaldense*. *J. Bacteriol.* **192**, 4192–4204 (2010).
28. Wang, Q. *et al.* Physiological characteristics of *Magnetospirillum gryphiswaldense* MSR-1 that control cell growth under high-iron and low-oxygen conditions. *Sci. Rep.* **7**, 2800 (2017).
29. Pereira, P. M. *et al.* Transcriptional response of *Desulfovibrio vulgaris* Hildenborough to oxidative stress mimicking environmental conditions. *Arch. Microbiol.* **189**, 451–461 (2008).
30. Zhou, A. *et al.* Hydrogen peroxide-induced oxidative stress responses in *Desulfovibrio vulgaris* Hildenborough. *Environ. Microbiol.* **12**, 2645–2657 (2010).
31. Caffrey, S. M. & Voordouw, G. Effect of sulfide on growth physiology and gene expression of *Desulfovibrio vulgaris* Hildenborough. *Antonie Van Leeuwenhoek* **97**, 11–20 (2010).
32. Ho, T. D. & Ellermeier, C. D. Ferric Uptake Regulator Fur Control of Putative Iron Acquisition Systems in *Clostridium difficile*. *J. Bacteriol.* **197**, 2930–2940 (2015).

Figures

Fig. 1: Proteins enriched with ferrosomes are essential for ferrosome formation. a, Five proteins most highly enriched in isolated ferrosomes compared to the cell lysate as detected by LC-ESI/MS: DMR_28320-40 (uncharacterized proteins), DMR_43090 (OmpA family), and DMR_12700 (AccC). Data presented are averages of three technical replicates (circles); error bars show s.d. **b**, DMR_28320-40 are encoded by genes arranged in a putative operon. Below, a schematic of FezB shows the conserved actuator and ATP-binding domains found in all P_{1B}-ATPases and six putative transmembrane domains (rectangles). Signature motifs in the N-terminal domain and predicted transmembrane domains are shown. Details of this schematic are based on alignments in Extended Data Fig. 3. **c-e**, *D. magneticus* strains one hour after transitioning out of iron starvation: WT (**c**, inset), Δ*fezBC* (**d**, inset), and Δ*fezBC::fezABC* (**e**, inset). White carets indicate magnetosomes, which have a bullet or diamond shape that is distinguishable from ferrosomes[6]. Scale bars, 200 nm; insets, 100 nm. **f,** Maximum diameter of individual ferrosomes (circles) in *D. magneticus* WT and Δ*fezBC::fezABC* strains. The bar indicates the mean maximum diameter. **g**, A maximum likelihood tree shows the relationship of FezB with other P_{1B}-ATPases. The FezB signature motif in the putative metal-binding transmembrane domain distinguishes it from other subgroups of P_{1B}-ATPases (color ranges). The internal black color strip indicates the presence of an N-terminal R-rich motif. The external color strip phylum or superphylum of organisms with a FezB homolog is indicated with the. The tree is rooted with KdpB (asterisk) and the collapsed clades contain P_{1B}-ATPases, including CopA, CopB, ZntA, and PfeT. Bootstraps >70% are indicated with black circles. **h,** Genes encoding FezB are found in genomic regions with additional conserved genes that encode proteins with GxxxG motifs—or, less frequently, GxxxA motifs—proteins with HMA/DUF4405 domains, and proteins with a possible role in iron homeostasis.

Fig. 2: *fez* genes are essential for ferrosome formation and function in *S. putrefaciens*. a, The *S. putrefaciens* six gene *fez* operon. Gene colors correspond to Fig. 1h. **b-d**, Micrographs of *S. putrefaciens* strains grown with HFO: WT (**b**, inset), Δfez_{Sp} (**c**, inset), and Δfez_{Sp}::fez_{Sp} (**d**, inset). White arrows indicate ferrosomes. Scale bars, 200 nm; insets, 100 nm. **e,** Lag between strains was inferred by determining the time at which each culture reached the 1/2 maximum OD_{595}. Each data point represents an independent culture. Each bar indicates the mean from six

independent cultures. The data represented here is shown in Extended Data Fig. 9b. **f,** Growth curves of *S. putrefaciens* strains grown anaerobically with 0 μM EDTA or 100 μM EDTA. **g,** Growth curves of *S. putrefaciens* strains grown anaerobically with 0 μM EDTA/100 μM $FeSO_4$ or 100 μM EDTA/100 μM $FeSO_4$. Legend shown in **f** also applies to **g**. Data presented are averages of three independent cultures (technical replicates); error bars indicate s.d.

Fig. 3: *fez* genes enable ferrosome formation in foreign hosts. WT *E. coli* cell pellets when grown anaerobically in the absence (**a**) or presence (**b**) of iron supplementation. *E. coli* fez_{Sp}^{+} cell pellets when grown anaerobically in the absence (**c**) or presence (**d**) of iron supplementation. **e-g**, Micrographs of *E. coli* strains grown anaerobically in growth medium supplemented with iron. WT *E. coli* harboring a control plasmid (**e**) and *E. coli* fez_{Sp}^{+} (**f, g**). Electron dense granules are indicated with arrows. Scale bars, 100 nm (**e, f**); 50 nm (**g**). **h, i**, EDS spectra of an area in an *E. coli* cell with a control plasmid (**h**) and an area in an *E. coli* fez_{Sp}^{+} cell containing ferrosomes (**i**). The red asterisk indicates the iron peak. **j, k**, Micrographs of WT *M. magneticum* (**j**) and *M. magneticum* fez_{Rp}^{+} (**k**). Magnetosomes are denoted with white carets. Yellow circles indicate areas containing one or more putative ferrosomes. Black circles indicate areas containing granules that are difficult to distinguish from magnetosomes due to their proximity to the magnetosome chain. Scale bars, 100 nm. **l**, Maximum feret diameter of ferrosomes measured in the *S. putrefaciens* (Sp) and *R. palustris* (Rp) WT strains and Δ*fez* mutants complemented with their respective *fez* operon, *E. coli* (Ec) fez_{Sp}^{+}, and *M. magneticum* (Mm) fez_{Rp}^{+}. Each data point represents one ferrosome and each bar indicates the mean maximum diameter.

Methods

Strains, media, and growth conditions. The bacterial strains used in this study are listed in Supplementary Table 8. All aerobic cultures were grown with continuous shaking at 250 rpm. Anaerobic cultures and plates were grown at 30°C in an anaerobic glovebox or in sealed Balch tubes with a N_2 headspace containing medium that was degassed with N_2. Ferrous iron stocks were prepared by dissolving 1 M $FeSO_4$ in 0.1 N HCl, which was subsequently stored in an anaerobic glovebox. Stocks of ferric malate were prepared as 20 mM $FeCl_3$/60 mM malate, unless otherwise stated. If needed, nitrilotriacetic acid (NTA) disodium salt was added to the ferrous iron just before use to prevent precipitation of iron in the growth medium[33]. NTA alone did not affect cellular growth.

D. magneticus strains were grown at 30°C anaerobically in RS-1 growth medium (RGM), as described previously[6,10]. For growth in iron replete medium, 100 μM ferric malate was added to RGM prior to inoculation. For growth in iron limited medium (IL-RGM), iron was omitted from RGM and all glassware was soaked in oxalic acid for one to two days, as described previously[6]. To starve cells of iron, cultures were passaged in IL-RGM, as described previously[6], or washed with IL-RGM prior to inoculation. To induce ferrosome formation, iron-starved cells were grown anaerobically in IL-RGM until they reached an OD_{650} ~0.1, at which point ferric malate was added to the cultures at a concentration of 100 μM[6].

S. putrefaciens strains were grown aerobically at 30°C in Luria-Bertani (LB) broth or anaerobically at 30°C in LB broth supplemented with 10 mM lactate and 10 mM fumarate or hydrous ferric oxide (HFO). HFO was prepared as described previously[7]. As needed, 1 mM ferrous iron and 2 mM NTA, 100 μM ferrous iron, or 100 μM ferric malate was added to the anaerobic growth medium.

R. palustris strains were grown at 30°C aerobically in the dark in YP medium (0.3% yeast extract and 0.3% peptone) or anaerobically in photoheterotrophic medium (PM) supplemented with 10 mM succinate (PMS-10), as described previously[34]. Anaerobic cultures were incubated in a growth chamber with constant light (100 μE of photosynthetically active radiation). As needed, 1 mM ferrous iron was added to the anaerobic growth medium. Because *R. palustris* can oxidize ferrous iron, 3.4 mM citrate trisodium dihydrate was added to prevent ferric iron precipitates from accumulating in the growth medium[35].

E. coli strains were grown aerobically at 37°C in LB or anaerobically at 30°C in M9 minimal medium supplemented with 0.4% glucose and 20 mM fumarate. For anaerobic growth, 285 μM L-cysteine was added as a reducing agent. As needed, the anaerobic medium was supplemented with iron (1 mM ferrous iron and 2 mM NTA) or without iron (0.1 mN HCl and 2 mM NTA).

M. magneticum strains were cultured in *Magnetospirillum* growth (MG) medium containing Wolfe's vitamins[36,37]. 30 μM iron was added from a stock of 3 mM $FeCl_3$/9 mM malate. Cells were grown in tubes filled with MG medium to the top and incubated in a 30°C incubator, as described previously[37]. For growth on solid media, 0.7% agar was added and plates were incubated at 30°C in a sealed jar with 7% oxygen.

Antibiotics and selective reagents used are as follows: kanamycin (50 μg/mL for *E. coli* and *S. putrefaciens* strains, 125 μg/ml for *D. magneticus*, 200 μg/ml for *R. palustris*, and 7 μg/ml in liquid cultures and 10 μg/ml in solid media for *M. magneticum*), streptomycin (50 μg/ml for *E. coli* and *D. magneticus* strains), diaminopilmelic acid (DAP) (300 μM for *E. coli* WM3064), and sucrose (10% for *R. palustris* and *S. putrefaciens*, 1% for *D. magneticus*).

Plasmids and cloning. Plasmids used in this study are listed in Supplementary Table 9. In-frame deletion vectors targeting fez_{Rp} and fez_{Sp} were constructed by amplifying upstream and downstream homology regions from *R. palustris* strain CGA009 and *S. putrefaciens* strain CN-32 genomic DNA, respectively, using the primers listed in Supplementary Table 10. The homology regions were then inserted into the SpeI site of pAK31 using the Gibson cloning method. The deletion vector for $fezBC_{Dm}$ was constructed by amplifying upstream and downstream homology regions from *D. magneticus* strain AK80 genomic DNA using the primers listed in Supplementary Table 10. The P_{npt}-*strAB* cassette was subsequently ligated between the upstream and downstream homology regions of the deletion vector via BamHI. Expression plasmids for fez_{Rp} and fez_{Sp} were constructed by amplifying the respective gene cluster using the primers listed in Supplementary Table 10. The amplified DNA was inserted into HindIII/SpeI-digested pAK22 via the Gibson cloning method. The $\Delta fezBC_{Dm}$ complementation vector was constructed by amplifying P_{fez}-*fezABC* from *D. magneticus* genomic DNA using the primers listed in Supplementary Table 10. The amplified DNA was then ligated into the SalI/XbaI sites of the expression vector pBMK7.

Plasmids were transformed into *E. coli* WM3064 and then transferred to *D. magneticus*, *S. putrefaciens*, *R. palustris*, or *M. magneticum* via conjugation. For *D. magneticus*, conjugations were performed as described previously[10]. Allelic replacement of $fezBC_{Dm}$ (*dmr_28330-40*) with *strAB* was achieved with streptomycin selection and sucrose counterselection as described previously[9]. Attempts to isolate a $fezABC_{Dm}$ mutant with this method were unsuccessful. Conjugal transfer of plasmids to *R. palustris* were performed as described previously[21,38]. Transconjugants were selected on YP plates with 100 μg/ml kanamycin. For conjugal transfer of plasmids to *S. putrefaciens*, overnight cultures of *S. putrefaciens* and *E. coli* WM3064 carrying

the plasmid to be transferred were mixed, spotted on LB agar plates containing DAP, and incubated aerobically at 30°C for 1 day. Transconjugants were selected with 50 μg/ml kanamycin. Δfez_{Rp} and Δfez_{Sp} candidates were selected on 10% sucrose plates and screened for kanamycin sensitivity. Deletions were also confirmed by PCR. Conjugal transfer of plasmids to *M. magneticum* were performed as described previously and transconjugants were selected on MG agar plates with 10 μg/ml kanamycin[36,37].

Ferrosome isolation. *D. magneticus* was grown anaerobically in IL-RGM. Cells were then passaged 1:400 into two liters of anaerobic IL-RGM as described above. When the culture reached an OD_{650} ~0.1, 100 μM ferric malate was added. After three hours, cells were pelleted at 8,000xg for 20 minutes and flash froze in liquid nitrogen before storing at -80°C. Samples were observed by TEM before and after the addition of iron to ensure ferrosomes had formed. We found that this method enriches for both ferrosomes and magnetosomes (Extended Data Fig. 2a-c). In order to prevent contamination with magnetosomes and magnetosome proteins, we isolated ferrosomes from a magnetosome gene island deletion strain, ΔMAI, and prepared the samples for proteomics.

Cell pellets were thawed on ice and resuspended with ice-cold LyA buffer (10 mM Tris HCl pH 8.0, 50 mM NaCl, and 1 mM EDTA) containing 250 mM sucrose, 1 μg/ml leupeptin and pepstatin A and 1 mM PMSF. Cells were lysed by passage through a French pressure cell three times. The lysate was then passed through a 0.2 μm filter to remove unlysed cells. The filtered cell lysate was gently layered over a 65% sucrose cushion and centrifuged at 35,000 rpm at 4°C for 2h. The resulting pellet was resuspended in 1 ml of LyA supplemented with leupeptin,

pepstatin, and PMSF and washed two times with LyA before resuspending in a final volume of 50 μl.

Liquid chromatography-mass spectrometry. Isolated ferrosomes (5 μg) and whole cell lysate (50 μg) were prepared for liquid chromatography-mass spectrometry (LC-MS) analysis as described previously[39]. Trypsin-digested protein samples were each analyzed in triplicate using an Acquity M-class ultra-performance liquid chromatography (UPLC) system that was connected in line with a Synapt G2-Si mass spectrometer that was equipped with a nanoelectrospray ionization source (Waters, Milford, MA). The UPLC system was equipped with trapping (Symmetry C18, inner diameter: 180 μm, length: 20 mm, particle size: 5 μm) and analytical (HSS T3, inner diameter: 75 μm, length: 250 mm, particle size: 1.8 μm) columns (Waters). Ion mobility-enabled, high-definition mass spectra and tandem mass spectra were acquired in a data-independent manner in the positive ion mode[40-42]. Data acquisition was controlled using MassLynx software (version 4.1), and tryptic peptide identification and relative protein quantification using a label-free approach[43-45] were performed using Progenesis QI for Proteomics software (version 4.0, Nonlinear Dynamics/Waters). This methodology has been used previously in similar experiments[46-49]. Raw data were searched against the *Desulfovibrio magneticus* strain RS-1 translated protein database, in FASTA format, to identify tryptic peptides. A list of all proteins identified is available in Supplementary Table 11.

Electron microscopy. Whole-cell transmission electron microscopy was performed as described previously[6]. All TEM was done using the Tecnai 12 at the EM-Lab at the University of

California, Berkeley. Ferrosomes were measured with the Analyze Particles tool in ImageJ (1.52q)[50].

Chemical composition of ferrosomes. Ferrosome-containing and ferrosome-free *E. coli* and *S. putrefaciens* strains were deposited on copper grids coated with a formvar carbon membrane. The chemical composition of ferrosomes was investigated from Energy Dispersive X-ray Spectroscopy (EDS, Oxford X-max 80T detector) using a transmission electron microscope (FEI Tecnai G2 operating at 200 kV). EDS spectra were acquired under Scanning TEM (STEM) mode.

***S. putrefaciens* growth tests**. For aerobic growth tests, *S. putrefaciens* WT and Δfez_{Sp} strains grown aerobically overnight were used as an inoculum at a 1:1000 dilution. For anaerobic growth tests, *S. putrefaciens* strains grown anaerobically to stationary phase were used as an inoculum at a 1:200 dilution. For all anaerobic growth assays, LB was supplemented with lactate (10 mM) and fumarate (10 mM) and the precultures and experiments were set up and performed inside an anaerobic glovebag. For the complementation assays shown in Fig. 2f, g, WT and Δfez_{Sp} (both carrying the control plasmid pBBR1MCS-2) and Δfez_{Sp}::fez_{Sp} were inoculated in anaerobic LB supplemented with lactate, fumarate, and kanamycin. The 96-well plates were sealed with a Breathe-Easy (Diversified Biotech) membrane seal and incubated at 30°C with continuous shaking and growth was monitored by measuring the A_{595} at 15 minute intervals in a Sunrise microplate reader (Tecan) controlled with Magellan™ software.

For each plate assay the early time points returned values that were below the detection limit and there was variability of the baseline reading among the wells, similar to what was described

444 in a recent study[51]. To account for this variability, we normalized the data by subtracting the
445 average of the first four measurements of each well from each timepoint in the corresponding
446 well. To account for evaporation effects on the data, we next subtracted the average of three or
447 four blank wells, which contained the growth medium and no inoculum, from each measurement
448 over the time course. One sample, Δ*fez*$_{Sp}$::*fez*$_{Sp}$ grown with 100 μM EDTA, was omitted from
449 further analysis due to noise throughout the time course. The lag in growth growth was inferred
450 by calculating the time at which each strain reached the ½ maximal OD_{595}. To determine the
451 growth rate, the slope of the natural log of the OD_{595} versus time over a sliding window of 7 time
452 points was calculated. Graphs displaying the growth curves, lag times, and growth rates were
453 made using Graphpad Prism (versions 8 and 9). The raw data is provided as Supplementary Data
454 1.
455
456 **Multiple sequence alignments and tree construction.** Unique protein sequences were obtained
457 by searching DMR_28330 and selected subsequent target sequences against all isolates in
458 IMG/M ER[52]. Representative P_{1B}-ATPase sequences from the characterized subgroups 1-4—
459 CopA, ZntA, CopB, and PfeT, as well as a P_{1A}-ATPase, KdpB—were also included. Sequences
460 were aligned using MUSCLE in MEGA (7.0.26)[53], with a gap open penalty of -6.9 and the
461 resulting alignment was trimmed using Gblocks[54]. The trimmed alignment was used to generate
462 a phylogeny using RAxML[55] with the LG+G+F model (determined using SMS[56]) and 100
463 bootstraps. The tree was rooted with KdpB and visualized and annotated using iTol[57].
464 To examine the synteny of *fez* gene clusters, we compiled a database of 304 FezB homologs
465 identified in our phylogenetic analysis and the proteins encoded by the ten genes upstream and
466 downstream of *fezB* for each species. We performed an all-versus-all search of these proteins

using mmseqs2 10.6d92c[58] (-s 7.5, -c 0.4, -e 1). The results from this search were uploaded into Cytoscape[59] with an e-value cutoff <0.01 to generate a sequence similarity network. The Kyoto Encyclopedia of Genes and Genomes (KEGG)[60] was used to identify conserved *fez* gene clusters containing FezB homologs (Extended Data Fig. 5a). These proteins were then mapped to nodes in eight different groups in the sequence similarity network. The Cytoscape plugin ClusterMaker[61] was used to subdivide the following groups through Markov Clustering (MCL) with the inflation value set to 1.5. Group 1 (-log(e-value) 100); group 2 (-log(e-value) 2.5); and group 3 (-log(e-value) 5). Each group and subgroup with three or more proteins was then aligned with Clustal Omega[62]. For each alignment, HMMER 3.1b2 was used to build a hidden Markov model which was searched against our database[63,64]. Subgroups that shared hits below a threshold of $1e^{-20}$ were merged and realigned. These alignments revealed a conserved GxxxG motif (or, less frequently, Gxxx[A/S] motif) for proteins in Groups 2 and 5 and an R-rich motif for proteins in Groups 1 and 3. Putative transmembrane domains were identified with TOPCONS 1.0[65]. Sequence logos of R-rich and GxxxG motif-containing proteins were generated with WebLogo[66].

Data availability. The mass spectrometry proteomics data have been deposited to the ProteomeXchange Consortium via the PRIDE[67] partner repository with the dataset identifier PXD017470. Ferrosome-associated proteins presented in Fig. 1a were identified from the data in Supplementary Table 11. The sequences, alignment, and tree data used to generate Fig. 1g are provided as Supplementary Data 2. KEGG[60] and IMG/M ER[52] were used to collect data.

Methods References

33. Jiao, Y. & Newman, D. K. The *pio* Operon Is Essential for Phototrophic Fe(II) Oxidation in *Rhodopseudomonas palustris* TIE-1. *J. Bacteriol.* **189**, 1765–1773 (2007).

34. Kim, M.-K. & Harwood, C. S. Regulation of benzoate-CoA ligase in *Rhodopseudomonas palustris*. *FEMS Microbiol. Lett.* **83**, 199–203 (1991).

35. Guan, G. *et al.* PfeT, a P_{1B4}-type ATPase, effluxes ferrous iron and protects *Bacillus subtilis* against iron intoxication. *Mol. Microbiol.* **98**, 787–803 (2015).

36. Komeili, A., Vali, H., Beveridge, T. J. & Newman, D. K. Magnetosome vesicles are present before magnetite formation, and MamA is required for their activation. *Proc. Natl. Acad. Sci. U. S. A.* **101**, 3839–3844 (2004).

37. Murat, D., Quinlan, A., Vali, H. & Komeili, A. Comprehensive genetic dissection of the magnetosome gene island reveals the step-wise assembly of a prokaryotic organelle. *Proc. Natl. Acad. Sci. U. S. A.* **107**, 5593–5598 (2010).

38. Rey, F. E., Oda, Y. & Harwood, C. S. Regulation of Uptake Hydrogenase and Effects of Hydrogen Utilization on Gene Expression in *Rhodopseudomonas palustris*. *J. Bacteriol.* **188**, 6143–6152 (2006).

39. Clark, I. C. *et al.* Synthetic and Evolutionary Construction of a Chlorate-Reducing *Shewanella oneidensis* MR-1. *mBio* **6**, (2015).

40. Plumb, R. S. *et al.* UPLC/MS^E; a new approach for generating molecular fragment information for biomarker structure elucidation. *Rapid Commun. Mass Spectrom.* **20**, 1989–1994 (2006).

41. Geromanos, S. J., Hughes, C., Ciavarini, S., Vissers, J. P. C. & Langridge, J. I. Using ion purity scores for enhancing quantitative accuracy and precision in complex proteomics samples. *Anal. Bioanal. Chem.* **404**, 1127–1139 (2012).

42. Shliaha, P. V., Bond, N. J., Gatto, L. & Lilley, K. S. Effects of traveling wave ion mobility separation on data independent acquisition in proteomics studies. *J. Proteome Res.* **12**, 2323–2339 (2013).
43. Levin, Y. & Bahn, S. Quantification of Proteins by Label-Free LC-MS/MS. In: Cutillas, P. R. & Timms, J. F. (eds.) *LC-MS/MS in Proteomics*, Methods in Molecular Biology **658**, 217–231, Humana Press, Totowa, NJ (2010).
44. Neilson, K. A. *et al.* Less label, more free: Approaches in label-free quantitative mass spectrometry. *Proteomics* **11**, 535–553 (2011).
45. Nahnsen, S., Bielow, C., Reinert, K. & Kohlbacher, O. Tools for label-free peptide quantification. *Mol. Cell. Proteomics* **12**, 549–556 (2013).
46. Light, S. H. *et al.* A flavin-based extracellular electron transfer mechanism in diverse Gram-positive bacteria. *Nature* **562**, 140–144 (2018).
47. Engström, P. *et al.* Evasion of autophagy mediated by Rickettsia surface protein OmpB is critical for virulence. *Nat. Microbiol.* **4**, 2538–2551 (2019).
48. Pinals, R. L. *et al.* Quantitative protein corona composition and dynamics on carbon nanotubes in biological environments. *Angew. Chem. Int. Ed.* **59**, 23668–23677 (2020).
49. Engström, P., Burke, T. P., Tran, C. J., Iavarone, A. T. & Welch, M. D. Lysine methylation shields an intracellular pathogen from ubiquitylation and autophagy. *Sci. Adv.* **7**, eabg2517 (2021).
50. Schneider, C. A., Rasband, W. S. & Eliceiri, K. W. NIH Image to ImageJ: 25 years of image analysis. *Nat. Methods* **9**, 671–675 (2012).
51. Atolia, E. *et al.* Environmental and Physiological Factors Affecting High-Throughput Measurements of Bacterial Growth. *mBio* **11**, (2020).

52. Chen, I.-M. A. *et al.* IMG/M v.5.0: an integrated data management and comparative analysis system for microbial genomes and microbiomes. *Nucleic Acids Res.* **47**, D666–D677 (2018).
53. Kumar, S., Nei, M., Dudley, J. & Tamura, K. MEGA: A biologist-centric software for evolutionary analysis of DNA and protein sequences. *Brief. Bioinform.* **9**, 299–306 (2008).
54. Castresana, J. Selection of conserved blocks from multiple alignments for their use in phylogenetic analysis. *Mol. Biol. Evol.* **17**, 540–552 (2000).
55. Stamatakis, A. RAxML version 8: a tool for phylogenetic analysis and post-analysis of large phylogenies. *Bioinformatics* **30**, 1312–1313 (2014).
56. Lefort, V., Longueville, J.-E. & Gascuel, O. SMS: Smart Model Selection in PhyML. *Mol. Biol. Evol.* **34**, 2422–2424 (2017).
57. Letunic, I. & Bork, P. Interactive Tree Of Life (iTOL) v4: recent updates and new developments. *Nucleic Acids Res.* doi:10.1093/nar/gkz239.
58. Steinegger, M. & Söding, J. MMseqs2 enables sensitive protein sequence searching for the analysis of massive data sets. *Nat. Biotechnol.* **35**, 1026–1028 (2017).
59. Markiel, S. P. *et al.* Cytoscape: a software environment for integrated models of biomolecular interaction networks. *Genome Res.* **13**, 2498–504 (2003).
60. Kanehisa, M. & Goto, S. Kyoto Encyclopedia of Genes and Genomes. *Nucleic Acids Res.* **28**, 27–30 (2000).
61. Morris, J. H. *et al. clusterMaker*: a multi-algorithm clustering plugin for Cytoscape. *BMC Bioinformatics* **12**, (2011).
62. Sievers, F. *et al.* Fast, scalable generation of high-quality protein multiple sequence alignments using Clustal Omega. *Mol Syst Biol* **7**, (2011).

63. Finn, R. D., Clements, J. & Eddy, S. R. HMMER web server: interactive sequence similarity searching. *Nucleic Acids Res.* **39**, W29–W37 (2011).
64. Eddy, S. R. Accelerated Profile HMM Searches. *PLOS Comput. Biol.* **7**, e1002195 (2011).
65. Bernsel, A., Viklund, H., Hennerdal, A. & Elofsson, A. TOPCONS: consensus prediction of membrane protein topology. *Nucleic Acids Res.* **37**, W465-468 (2009).
66. Crooks, G. E. WebLogo: A Sequence Logo Generator. *Genome Res.* **14**, 1188–1190 (2004).
67. Perez-Riverol, Y. *et al.* The PRIDE database and related tools and resources in 2019: improving support for quantification data. *Nucleic Acids Res.* **47**, D442–D450 (2019).

Acknowledgements We thank faculty at the EM-Lab at the University of California, Berkeley for their assistance with TEM; Andrea Campos for assistance with the EDS measurements; Kristen LeGault and Hayley McCausland for their help with conjugations in *R. palustris* and *M. magneticum*; Jeffrey Gralnick for providing *S. putrefaciens* strain CN-32; and the Coates lab and the Niyogi lab for sharing equipment. The QB3/Chemistry Mass Spectrometry Facility at the University of California, Berkeley received support from the National Institutes of Health (shared instrumentation grant 1S10OD020062-01). Research reported in this publication was supported by funding from the National Institutes of Health (R01GM084122 and R35GM127114), the Office of Naval Research (N000141310421), and the Bakar Fellows Program. H. A. T. is supported by the National Science Foundation Graduate Research Fellowship Program under Grant Number DGE 1752814. M. A. is supported by a grant through the *Fondation pour la Recherche Médicale* (ARF201909009123).

Author contributions C.R.G. and A.K. conceived and designed the study. C.R.G. performed all molecular cloning, genetic manipulation, TEM, cellular fractionations, and sample preparations for LC-MS analyses. A.T.I. performed all LC-MS analyses. C.R.G. identified ferrosome-associated proteins A.T.I. and H.T. C.R.G. carried out the bioinformatic analyses and tree construction. M.A. performed the EDS experiments and analysis. C.R.G. performed all growth assays with assistance from S.K. C.R.G. and A.K. prepared the manuscript with input from S.K, A.T.I., H.T., and M.A.

Competing interests The authors declare no competing interests.

Additional information

Supplementary information The online version contains supplementary material.

Correspondence and requests for materials should be addressed to A.K.

Reprints and permission information is available at www.nature.com/reprints.

Extended data figures

Extended Data Fig. 1 Ferrosomes are visible by TEM in whole D. magneticus cells after transitioning from iron limited to iron replete conditions. *D. magneticus* cells initially grown without iron (a) are shown 0.5 (b), 1.5 (c), and 6 (d) hours after addition of 100 μM ferric malate. (e) The maximum diameter of ferrosomes represented in b-d. Each data point represents one ferrosome and the bar indicates the mean maximum diameter in nm. Micrographs of *D. magneticus* one hour after adding low to high concentrations of ferric malate—1 μM (f), 10 μM (g), 100 μM (h), and 1 mM (i)—to iron-starved cells. (j) The maximum diameter of ferrosomes

represented in f-i. Each data point represents one ferrosome and the bar indicates the mean maximum diameter in nm. Scale bars, 200 nm.

Extended Data Fig. 2 Isolation of ferrosomes and characteristics of associated proteins. (a) Ferrosomes from ΔMAI *D. magneticus* (left) and magnetosomes from WT *D. magneticus* (right) form a pellet through 65% sucrose. Transmission electron micrographs of the ferrosome pellet (b) and the magnetosome pellet (c). Scale bars, 100 nm. (d-f) Membrane domain predictions of ferrosome-associated proteins in *D. magneticus*. DMR_28320 (a), DMR_28330 (b), and DMR_28340 (c) have 1, 5-6, and 0-2 putative transmembrane domains, respectively, as predicted by various methods analyzed through TOPCONS 1.0[65].

Extended Data Fig. 3 Multiple sequence alignment of FezB with characterized P_{1B}-ATPases. Conserved functional motifs in the actuator domain and the ATP-binding domain are indicated with blue and purple stars, respectively. The CxxC and histidine-rich metal binding sites in the cytoplasmic N-terminal domain of ZntA, CopA, and CopB are boxed. Transmembrane regions, predicted using TOPCONS 1.0[65], are underlined for each sequence. Putative metal-binding sites in the transmembrane domains are indicated with black stars.

Extended Data Fig. 4 WT and Δ*fezBC D. magneticus* strains make ferrosomes in iron replete medium when expressing *fezABC* in *trans*. Transmission electron micrographs of WT (a) and Δ*fezBC* (b) strains with a control plasmid make magnetosomes (white carets) when grown in iron replete medium. When expressing *fezABC* in *trans*, both the WT (c) and Δ*fezBC* (d) strains make magnetosomes as well as ferrosomes when grown in iron replete medium. Areas of the cell containing one or more putative ferrosomes are indicated with yellow circles. Scale bars, 200 nm.

Extended Data Fig. 5 Sequence similarity network of proteins encoded by *fez* gene clusters and genes frequently found near *fez* gene clusters. (a) Conserved *fez* gene clusters that encode FezB homologs. Conserved genes within the clusters are colored black. Gene clusters were identified using the "Gene cluster" tool in KEGG for each FezB homolog, in bold: Dde_0495, Dde_0498, Thimo_2900, vfu_A02104, SMUL_2748, RPA2333, KN400_3199, DMR_28330, and EUBELI_00578. The second copy of FezB in *D. alaskensis*, Dde_0498, is not shown because it is not part of a predicted conserved gene cluster. (b, c) Sequence similarity network highlighting the proteins encoded by ten genes upstream and downstream of 304 FezB homologs. Each node represents a protein and edges represent protein similarities that meet the specified e-value cutoff. (b) Network containing *fez* gene cluster-encoded proteins. Each group (labeled 1-8) contains one or more proteins encoded by conserved genes identified in (a) which are represented by black nodes and are labeled. Proteins or domains with an annotated function are labeled. Groups of proteins were further divided into subgroups which were used to identify proteins with GxxxG motifs in groups 2 and 5 and proteins with R-rich motifs in groups 1 and 3 (see Methods). The proteins represented in this network and their group/subgroup are listed in Supplementary Tables 3-6. (c) Network of proteins encoded by genes that are frequently found upstream and downstream of *fez* gene clusters. Only groups of more than 30 proteins are shown and the protein or domain annotation is labeled. Proteins with a known role in iron homeostasis are common and include iron transporters (FeoA, FeoB, outermembrane siderophore receptors, and some ABC transporters) and regulators (Fur and DtxR). The proteins represented in this network are listed in Supplementary Table 7.

Extended Data Fig. 6 Consensus motifs and characteristics of proteins with R-rich and GxxxG motifs. Representative proteins encoded by *fez* gene clusters with (a) an R-rich motif or

(b) a GxxxG motif. Logo shows the consensus motif for the subgroup or group of proteins to which the representative protein belongs. Predicted protein structure schematics show approximate location of the R-rich motif, putative transmembrane helices, and GxxxG motif for each protein (not to scale).

Extended Data Fig. 7 Transmission electron micrographs of *S. putrefaciens* and *R. palustris*. WT *S. putrefaciens* (a, b) and *R. palustris* (c, d), Δfez_{Sp} (e, f), Δfez_{Rp} (g), Δfez_{Sp}::fez_{Sp} (h, i), and Δfez_{Rp}::fez_{Rp} (j). *S. putrefaciens* strains respiring fumarate in medium supplemented with 100 μM ferric malate (a, e, h) or 1 mM ferrous iron (b, f, i). *R. palustris* strains grown anaerobically (c, g, j) or aerobically (d). White arrows denote ferrosomes. Polyphosphate granules are indicated with white asterisks. Scale bars, 200 nm.

Extended Data Fig. 8 EDS spectra of *S. putrefaciens* and *E. coli*. EDS spectrum of an *S. putrefaciens* Δfez_{Sp} cell, which does not form ferrosomes. (b, c) EDS spectra of *S. putrefaciens* WT obtained from an area in the cell that contained ferrosomes (b) and an area that had no visible ferrosomes (c). The red asterisk indicates the iron peak associated with ferrosomes in WT *S. putrefaciens*. (d, e) Spectra of the background taken from areas of the *S. putrefaciens* WT (d) and Δfez_{Sp} (e) grids that contained no cells. (f) An EDS spectrum of *E. coli* fez_{Sp}^{+} obtained from an area in the cell that had no visible ferrosomes. (g, h) Spectra of the background taken from areas of the *E. coli* cells with a control plasmid (g) or *E. coli* fez_{Sp}^{+} (h).

Extended Data Fig. 9 Effect of EDTA on the growth of *S. putrefaciens*. (a) OD_{595} measurements over time of *S. putrefaciens* WT (navy) and Δfez_{Sp} (yellow) grown aerobically with the indicated concentrations of EDTA. Each line is the mean of 3 individual cultures (technical replicates); error bars indicate s.d. (b) OD_{595} measurements over time of *S. putrefaciens* WT (navy) and Δfez_{Sp} (yellow) grown anaerobically with the indicated

concentrations of EDTA. Each line is the mean of 6 individual cultures (2 biological replicates with 3 technical replicates, with the exception of 150 μM EDTA which had 2 technical replicates); error bars indicate s.d. (c) Growth rate versus OD_{595} of the individual cultures shown in (b). Each circle represents the growth rate for an individual culture.

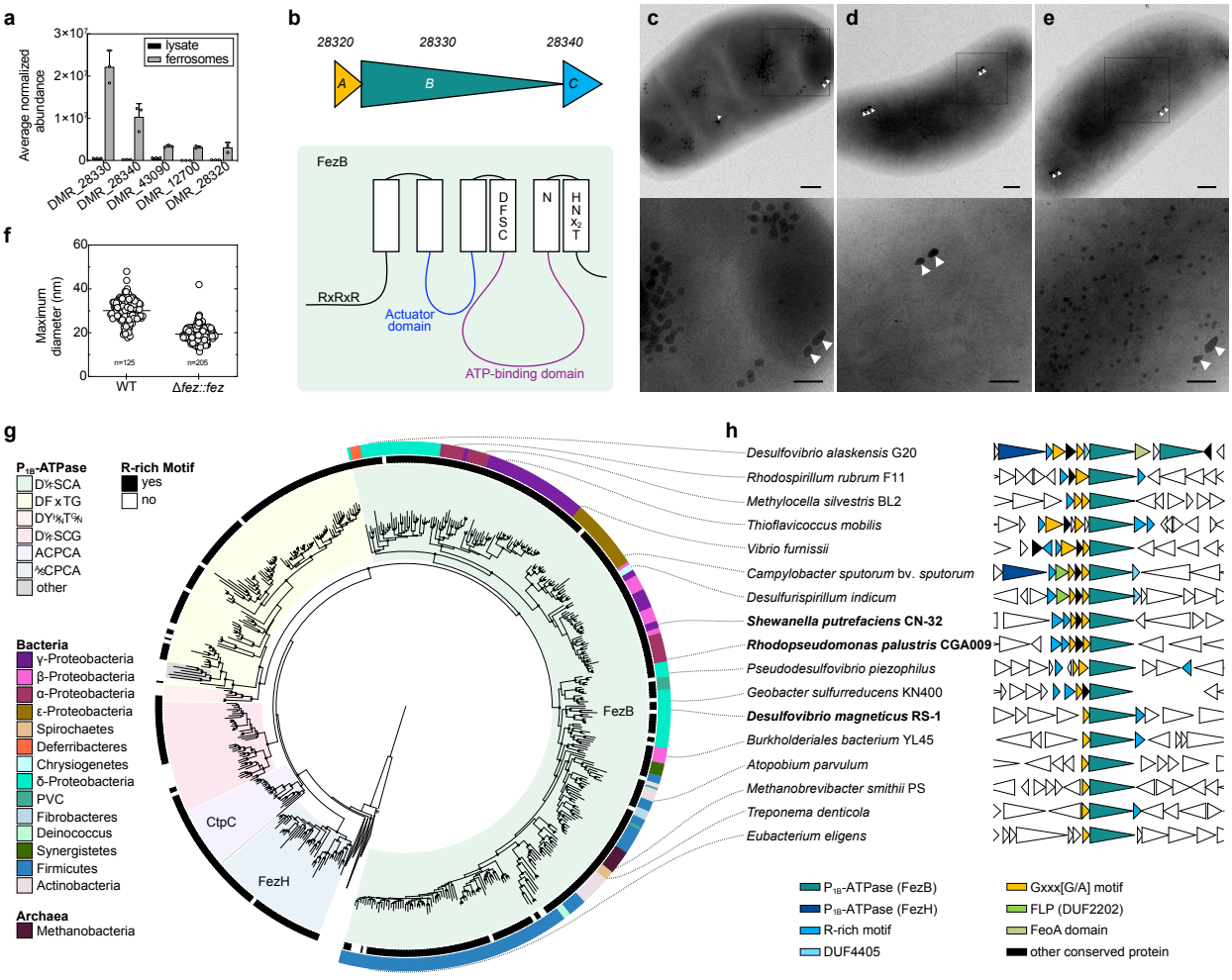
a
Average normalized abundance
lysate
ferrosomes
DMR_28330
DMR_28340
DMR_43090
DMR_12700
DMR_26320
b
28320
28330
28340
A
B
C
FezB
D
F
S
C
N
H
N
x2
T
RxRxR
Actuator domain
ATP-binding domain
c
d
e
f
Maximum diameter (nm)
n=125
n=205
WT
Δfez::fez
g
P1B-ATPase
DYSCA
DF x TG
DYXTY
DYSCG
ACPCA
XCPCA
other
R-rich Motif
yes
no
Bacteria
γ-Proteobacteria
β-Proteobacteria
α-Proteobacteria
ε-Proteobacteria
Spirochaetes
Deferribacteres
Chrysiogenetes
δ-Proteobacteria
PVC
Fibrobacteres
Deinococcus
Synergistetes
Firmicutes
Actinobacteria
Archaea
Methanobacteria
FezB
CtpC
FezH
h
Desulfovibrio alaskensis G20
Rhodospirillum rubrum F11
Methylocella silvestris BL2
Thioflavicoccus mobilis
Vibrio furnissii
Campylobacter sputorum bv. sputorum
Desulfurispirillum indicum
Shewanella putrefaciens CN-32
Rhodopseudomonas palustris CGA009
Pseudodesulfovibrio piezophilus
Geobacter sulfurreducens KN400
Desulfovibrio magneticus RS-1
Burkholderiales bacterium YL45
Atopobium parvulum
Methanobrevibacter smithii PS
Treponema denticola
Eubacterium eligens
P1B-ATPase (FezB)
P1B-ATPase (FezH)
R-rich motif
DUF4405
Gxxx[G/A] motif
FLP (DUF2202)
FeoA domain
other conserved protein

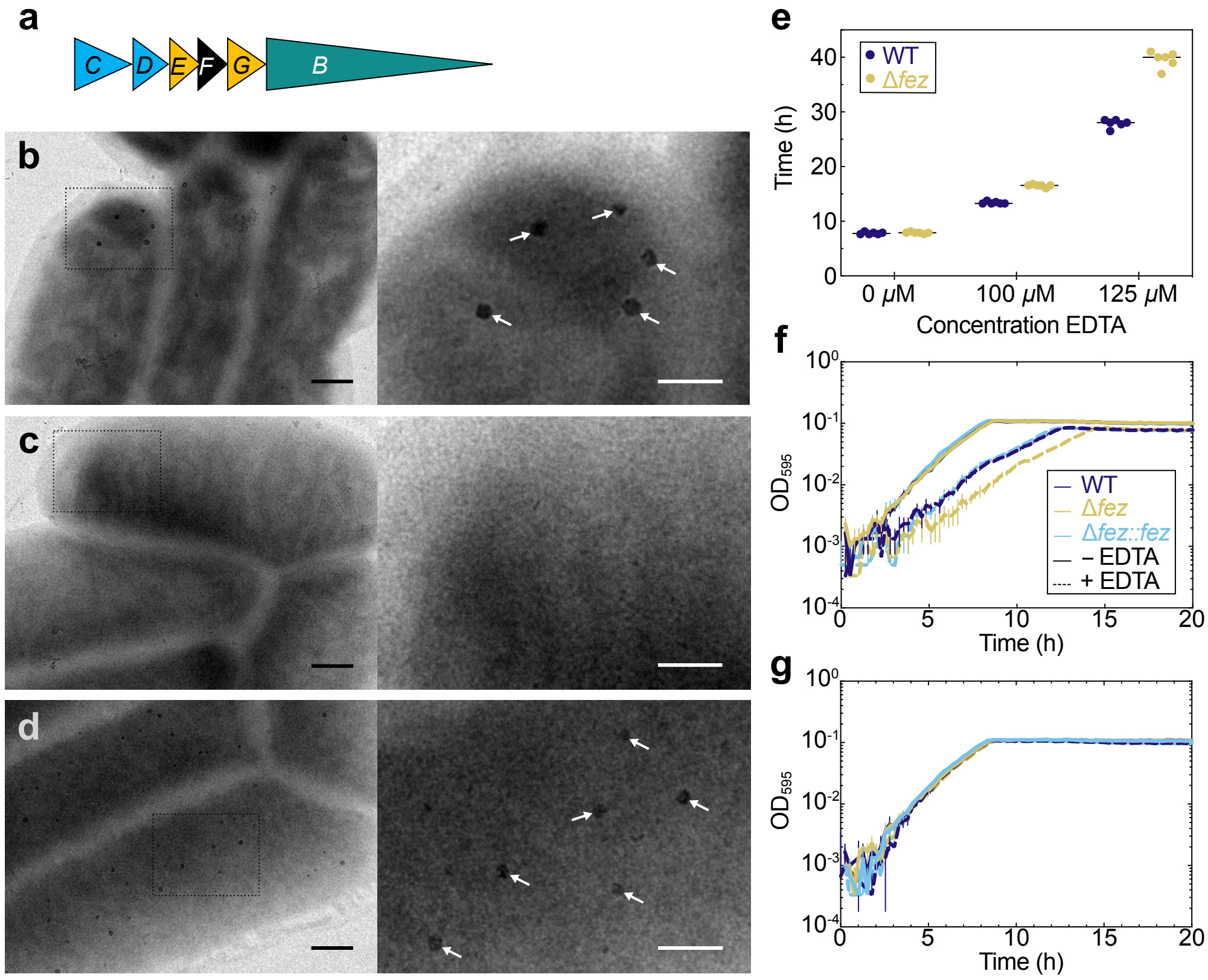
a
C
D
E
F
G
B
b
c
d
e
WT
Δfez
Time (h)
0
10
20
30
40
0 μM
100 μM
125 μM
Concentration EDTA
f
OD595
10^0
10^-1
10^-2
10^-3
10^-4
WT
Δfez
Δfez::fez
– EDTA
+ EDTA
0
5
10
15
20
Time (h)
g
OD595
10^0
10^-1
10^-2
10^-3
10^-4
0
5
10
15
20
Time (h)

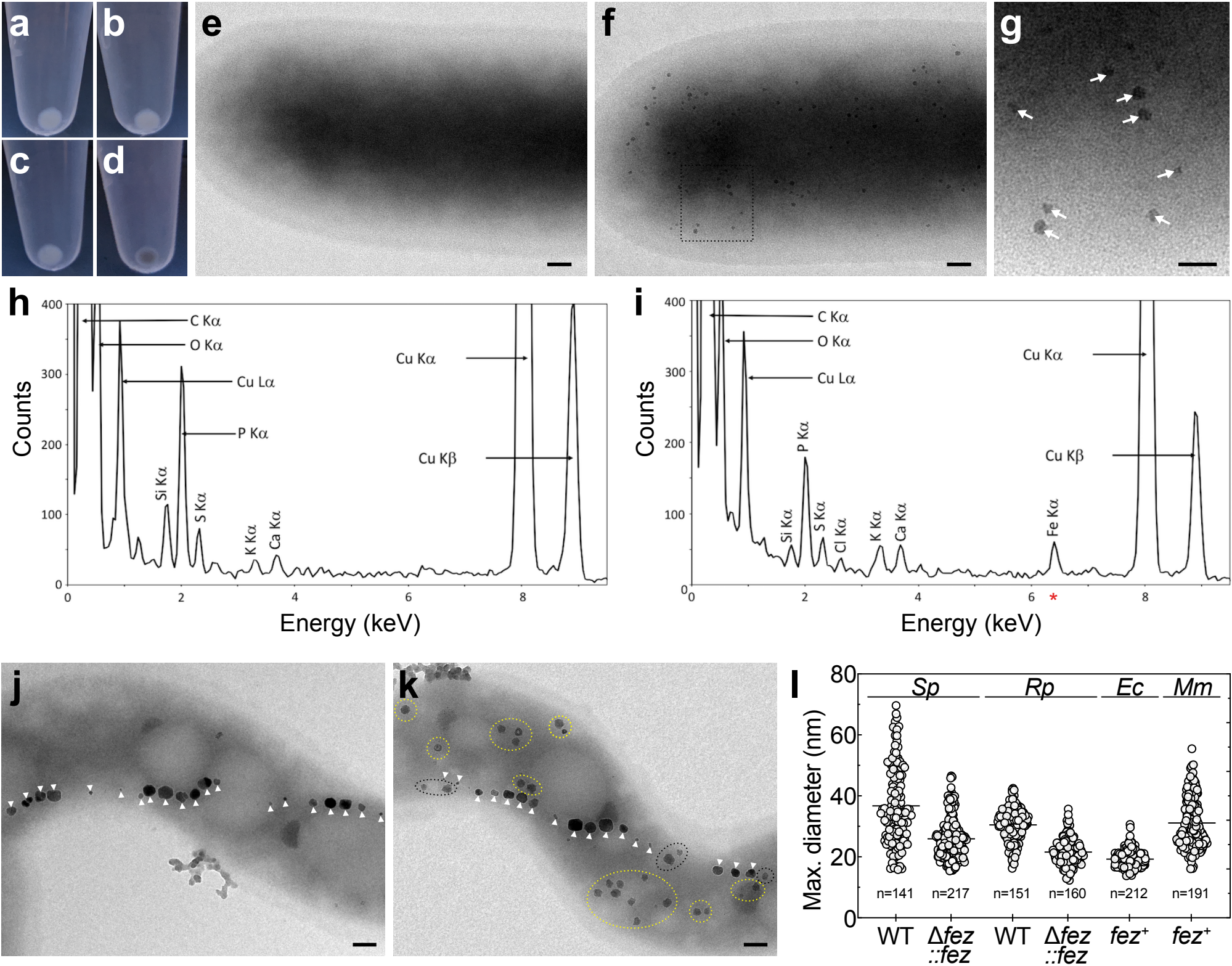
a
b
c
d
e
f
g
h
Counts
Energy (keV)
C Kα
O Kα
Cu Lα
P Kα
Si Kα
S Kα
K Kα
Ca Kα
Cu Kα
Cu Kβ
i
Counts
Energy (keV)
C Kα
O Kα
Cu Lα
P Kα
Si Kα
S Kα
Cl Kα
K Kα
Ca Kα
Fe Kα
Cu Kα
Cu Kβ
*
j
k
l
Max. diameter (nm)
Sp
Rp
Ec
Mm
n=141
n=217
n=151
n=160
n=212
n=191
WT
Δfez ::fez
WT
Δfez ::fez
fez+
fez+